An adapted hourly Himawari-8 fire product for China:principle, methodology and verification.

Jie Chen[1,★], Qiancheng Lv[2,★], Shuang Wu[3], Yelu Zeng[4], Manchun Li[5], Ziyue Chen[2] , Enze Zhou[6], Wei Zheng[1], Cheng Liu[2], Xiao Chen[2], Jing Yang[2], and Bingbo Gao[4]

[1]Key Laboratory of Radiometric Calibration and Validation for Environmental Satellites National Satellite Meteorological Center (National Center forSpace Weather), China Meteorological Administration and Innovation Center for FengYun Meteorological Satellite (FYSIC), Beijing 100081, China
[2]College of Global Change and Earth System Science, Beijing Normal University, Beijing 100091, China
[3]Heilongjiang Eco-Meteorology Center, Harbin,Heilongjiang 150030, China
[4]College of Land Science and Technology, China Agricultural University, Beijing 100083, China
[5]School of Geography and Ocean Science, Nanjing University, Nanjing 210023, China
[6]Electric Power Research Institute Gongdong Power Grid, Guangzhou, Guangdong 510000, China
★ These authors contributed equally to this work.

Correspondence to: Ziyue Chen (zychen@bnu.edu.cn) and Bingbo Gao (gaobingbo@cau.edu.cn)

Abstract. Wild fires exerts strong influences on the environment, ecology, economy and public security. However, the existing hourly Himawari-8 produced by Japan Meteorological Agency (JMA)JMA Himawari fire product presents large uncertainties and not suitable for reliable real-time fire monitoring in China. To fill this gap, National Satellite Meteorological Center (NSMC)we proposed an adaptive hourly Himawari-8NSMC Himawari fire product for China based on the original Himawari-8 source by employing a dynamical threshold for fire-extraction and a database of ground thermal sources. According to the visually-extracted reference and consistence check, we found NSMC-Himawari-8 fire product effectively removed a majority of false fire alarms included in the original Himawari-8JMA Himawari fire product. Based on a rare field-collected ground reference dataset, we evaluated the reliability of original Himawari-8JMA Himawari and NSMC-Himawari-8 fire product across China. The overall accuracy of raw Himawari-8JMA Himawari fire product was 54 % and 59 % (not considering the omission errors) respectively. As a comparison, by identifying more real fire pixels and avoiding a majority of false fire alarms, the overall accuracy of NSMC-Himawari-8 fire product was 80 % and 84 % (not considering the omission errors) respectively, making it an ideal source for improved real-time fire monitoring across China. This research also provides useful reference for employing local dataset of underlying surfaces and thermal sources to enhance the accuracy of global fire products in specific regions. NSMC-Himawari-8 fire product can be downloaded at http://figshare.com (last access: 16 March 202314 November 2022) with the identifier DOI: https://doi.org/10.6084/m9.figshare.21550248 (Chen et al., 2022).

1 Introduction

With a vast coverage, wild fires across China have a strong negative impact on crops (Song et al., 2022), forests (Ying et al., 2018; Ni1 et al., 2012; Zackrisson, 1977), grasslands (Balch et al., 2013), biodiversity (Driscoll et al., 2010; Andersen, et al., 2005), wildlife (Tiedemann et al., 2000), local and regional climate (Liu et al., 2018; Marlier et al., 2015) and public health (Huff et al., 2015; Johnston et al., 2012). Recently, increasing occurrence of annual forest fires in China has caused a large number of causality (Wu et al., 2014; Liu et al., 2012). The cross-country grassland fires, especially grasslands at the China-Mongolia boundary, are exerting an increasing serious threat to the sustainable development of grasslands (Na et al., 2018), the wealth (Abram et al., 2021; Cascio, 2018; Reid et al., 2016) and lives (Liu et al., 2015) of local residents. In addition to natural fires, anthropogenic fires, majorly the fires caused by crop-residue burning, which has been considered as one significant driver of airborne pollution (Li et al., 2015; Huang et al., 2012; Angassa and Oba, 2008) and strictly controlled across China, are given growing emphasis in recent years.

Given the significant role of wild fires in the national ecology, environment and economy, as well as people's daily, both the central and local governments are making substantial efforts on the preventing and controlling natural and human-induced fires (Panjaitan et al., 2019). Amongst a series of measures, the timely and precise monitoring is key for the effective identification and suppression of wild fires (Earl and Simmonds, 2018; Andela et al., 2017; Zhang et al., 2014). In the past, regular forest, farmland and grassland inspection is the major approach for preventing wild fires (Röder et al., 2008). However, this approach is highly resource-consuming and of extremely low efficiency (Giglio et al., 2006). Furthermore, for those distant regions with terrible natural conditions and scarce residents, it is difficult for people to conduct manual inspection. In that case, wild fires occur in these areas can hardly be detected within a short period. To address this issue, some alternative solutions have been employed. For instance, a large number of on-site monitoring sensors can be installed randomly in forests or grasslands to real-time capture the smoke and heat and thus quickly detect active fires (Li et al., 2019). However, massive resources are required for installing and maintaining these sensors. Meanwhile, there is still a majority of areas that cannot be covered by these sensors and thus the general efficiency and accuracy of fire monitoring remains low (Ichoku et al., 2012; Freeborn et al., 2011).

Thanks to its easy access, low cost, continuous time series and most importantly, large-scale and spatially continuous coverage, remote sensing has been increasingly employed for fire monitoring (Xu et al., 2017; Schmit et al., 2017). Since 1970s, National Oceanic and Atmospheric Administration (NOAA) series satellites (www.noaa.gov) and NOAA fire products, with a spatial resolution of 1.1 km and a daily temporal resolution, have been employed for global fire monitoring (Fuller and Fulk, 2018). Afterward, many regional or global fire products has been proposed in recent years. Attributed to its free access, long time series, and reliable accuracy (Giglio et al., 2018), Moderate Resolution Imaging Spectroradiometer (MODIS) fire product, with a spatial resolution of 1km and a temporal resolution of 12 hours, have become one of the most widely employed fire products since 2000 (Justice et al., 2002). Visible Infrared Imaging Radiometer Suite (VIIRS) fire products, with a temporal resolution of 12 hours and an improved spatial resolution of 375 m, has been available since 2011

(Schroeder et al., 2014). Despite a higher spatial resolution, the accuracy of VIIRS fire products is generally lower than that of MODIS fire products (Sharma et al., 2017). In recent years, China has launched a series of Fengyun series satellites, based on which a diversity of meteorological and fire products can be produced. We recently publicly released a Fengyun-3D global fire product (http://satellite.nsmc.org.cn/portalsite/default.aspx, Chen et al., 2022), with a daily resolution and 1km spatial resolution. Fengyun-3D fire product has a good global consistence with MODIS fire product and presented a significantly improved accuracy in China (Chen et al., 2022), making it an ideal continuity of MODIS fire products and a better choice for relevant study in China.

Despite the rapid development of daily-level and moderate-resolution global fire products, they are not suitable for quick identification of wild fires and understanding their environmental and ecological consequences (Yang et al., 2019). To fill this gap, specific satellites have been launched recently to produce fire products with extremely high temporal resolution. GEOS-16 Advanced Baseline Imager (ABI) fire products, with a temporal resolution of five minutes and a spatial resolution of 2 km, have been available for regional fire monitoring in ~~the western hemisphere~~Southeastern Conterminous United ~~States (CONUS) since 2017~~ (Hall et al., 2019). Himawari-8 products from Japan Meteorological Agency (JMA)~~-~~, with a spatial resolution of 2 km and temporal resolution of 10 minutes, have been employed to monitor meteorology and wild fires in Asia and Australia since 2015 (Xu and Zhong, 2017). Given its moderate spatial resolution, extremely high temporal resolution and its fixed observation region, Himawari-8 is quite suitable for real-time monitoring wild fires in China. Furthermore, compared with MODIS or Fengyun-3D fire products, which fail to capture the occurrence of in the night, Himawari-8 is advantageous of continuously monitoring wild-fires after sunset, which is highly suitable for replacing manual inspection to monitor wild fires in the night. However, existing Himawari-8 fire product presented a poor consistence with MODIS data (Jang et al., 2019) and the accuracy of Himawari-8 fire products in China remained unknown Without reliable accuracy report, Himawari-8 fire products, despite its good potential, have been limitedly employed (Na et al., 2018).

To provide a more reliable fire product for active fire monitoring in China, based on the raw Himawari-8 data, we proposed a new hourly fire product for China (National Satellite Meteorological Center Himawari-8 fire product for China, NSMC-Himawari-8 fire product for China) by employing adapted fire detection algorithms and local parameters concerning underlying surface and meteorological conditions, which were not available and implemented by JMA. This paper introduces the characteristics and fire detection algorithms of the new fire product (recently downloadable at http://figshare.com). Meanwhile, based on the ground-truth data, which is rarely collected and employed for verifying fire detection in China, we compared the accuracy of JMA-Himawari-8 and NSMC-Himawari-8 fire product. Thanks to its good spatiotemporal resolution and significantly improved accuracy, NSMC-Himawari-8 fire product has the potential to largely prompt the fire prevention and control and boost relevant ecological and environmental research in China.

2 Overview of Himawari-8 fire products

2.1 Instrument

Himawari−8 geostationary meteorological satellite was launched by the Japan Meteorological Agency (JMA) at the Tanegashima Space Center in October 2014, and officially began operation in July 2015 (Bessho et al., 2016). The satellite was designed to continuously support monitoring storm clouds, typhoon movements, volcanoes with continuous eruptions and other disaster prevention areas for more than 15 years. The sub satellite point is located over the equator at 140.7 ° E, with an operating altitude of approximately 35800 km. As a new generation of geostationary meteorological satellite, Himawari−8 with an improved Advanced Himawari-8 Imager (AHI) has a great improvement in observation frequency and spatial resolution compared with the previous satellites. AHI includes a total of 16 bands from visible light to far infrared (as shown in Table1), which can access the 500 m high spatial resolution in red band and support the observation time interval of 10 min. Himawari−8/AHI with six observation spots can monitor four regions in total, including the full disk (60° N-60° S, 80° E-160° W), Japan (scope of two Japanese regions), the tropical cyclone sensitive area (target area) and the corner of Australia (landmark area).

Table 1. Observation bands of Himawari−8.

Band	Wavelength (µm)	Waveband	Resolution (km)
1	0.470 63	Visible light	1
2	0.510 00	Visible light	1
3	0.639 14	Visible light	0.5
4	0.856 70	Near infrared	1
5	1.610 10	Near infrared	2
6	2.256 80	Near infrared	2
7	3.885 30	Thermal infrared	2
8	6.242 90	Thermal infrared	2
9	6.941 00	Thermal infrared	2
10	7.346 70	Thermal infrared	2
11	8.592 60	Thermal infrared	2
12	9.637 20	Thermal infrared	2
13	10.407 30	Thermal infrared	2
14	11.239 50	Thermal infrared	2
15	12.380 60	Thermal infrared	2

Formatted Table

| 16 | 13.280 70 | Thermal infrared | 2 |

2.2 Product overview

110 Thanks to Himawari−8/AHI's multi-band setting and the substantial improvement of high-frequency characteristics of observation, JMA has generated a wildfire data at a spatial resolution of nominal 0.02° (2 km x 2 km at nadir) and hourly temporal resolution (Wickramasinghe at al., 2016). This product has been widely used in wildfire monitoring and analysis in Asia and Australia (Y. Kurihara et al.,2020), with surprising results. This product provides the location and the fire radioactive power (FRP) of hot spots retrieved from the IR imageries carried on Himawari-8, using the retrieval algorithm

115 developed by Japan space agency Earth Observation Research Center (JAXA/EORC). Based on the notable difference of the brightness temperature between fire spots and background, this JMA fire detection algorithm can reliably monitor hot spots for the full disk (60° N-60° S, 80° E-160° W). And the reliability level of fire detection is given according to detection situations such as sun glint, solar angle, spatial variability of the brightness temperature, and so on. JMA--Himawari-8 fire product has extremely high temporal resolution and good accuracy in Japan (Wickramasinghe at al., 2016). However, given

120 the large variations in underlying surfaces and potential limitations of the fire detection algorithm, the reliability of JMA-Himawari-8 fire product across the entire monitoring region remains unclear (Liu at al., 2018). Specifically for China, in these years, increasing emphasis has been placed on the timely and reliably monitoring of wildfires, especially crop-residue burning, and the use of satellite data sources has been widely employed. However, the consistence between multiple mainstream fire products in China was relatively low (Liu at al., 2018), which caused large uncertainty and difficulty in

125 providing reliable reference for fire monitoring. With the highest temporal resolution, Himawari-8-based fire products have a great potential to support the real-time fire identification in China. Nevertheless, in practical implementation, JMA-Himawari-8 fire product seems to have a poor consistence with commonly employed MODIS fire product in China. Meanwhile, due to the lack of ground-truth reference, the accuracy of JMA-Himawari-8 fire product has yet been verified and the wide implementation of JMA-Himawari-8 fire product in China's fire monitoring has been limited.

130 To fully explore the advantage of Himawari−8/AHI for fire detection and overcome the potential limitation of JMA-Himawari-8 fire product, we presented a new hourly fire product from 2019 to 2021, NSMC-Himawari-8 fire product for China with an hourly temporal resolution and a spatial resolution of 2 km. By specifically considering the underlying surface information in China and adjusting fire detection algorithms, NSMC-Himawari-8 fire product aims to present an improved reliance for timely fire identification in China, which can provide fire location, burning area, intensity, district name and

135 distribution of underlying surfaces. As briefly demonstrated in Fig. 1, there is a large difference between the two products, characterized with many more fire pixels identified by JMA-Himawari-8 fire product.

The NSMC-Himawari-8 fire product has been produced to have a better accuracy than JMA-Himawari-8 fire product through the following strategies. Firstly, by considering the underlying surface information, conventional thermal anomalies caused by industrial production and photovoltaic power plants, which may be easily recognized as fires, can be effectively

140 avoided. Second, we dynamically adjusted the function of fire pixels identification threshold. As a comparison, commonly

employed fire-extraction algorithms used a fixed threshold when calculating the brightness temperature difference between the target pixel and the surrounding pixels, which may cause increased uncertainty for non-uniform underlying surface, where the difference of brightness temperature between the target pixel and surrounding pixels varied notably (Chen et al., 2022). Thirdly, we adopted a more efficient approach to calculate the background brightness temperature. For traditional

145 algorithms, due to the coarse resolution of underlying surface, the influence of vegetation type, vegetation coverage and cloud coverage cannot be fully considered. By including more reliable information of the underlying surface in China, our algorithm can better calculate the background brightness temperature of the target area.
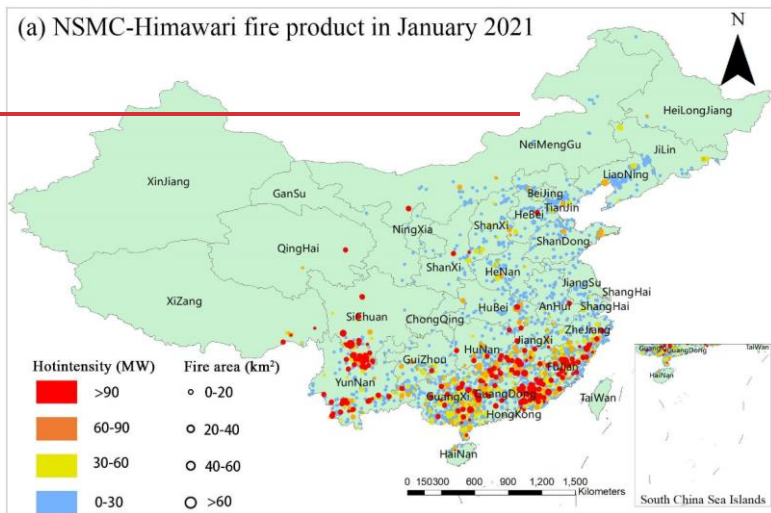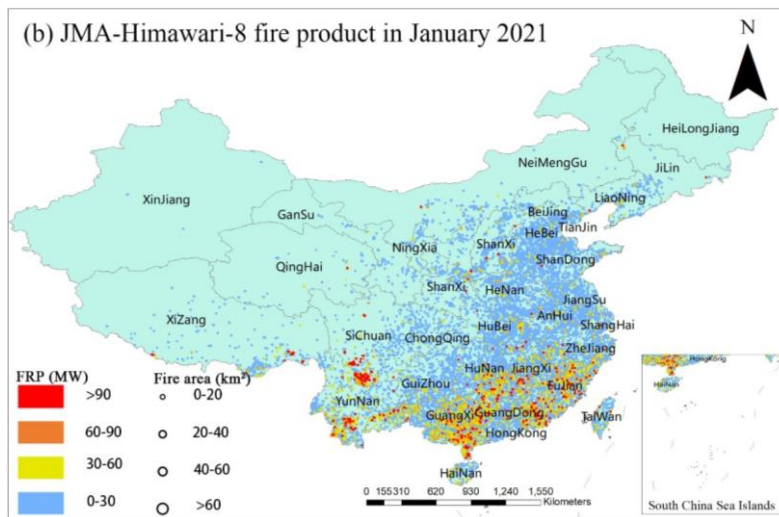
Figure 1: A brief illustration of JMA- Himawari-8 and NSMC-Himawari-8 fire product in January 2021.

3 Methods

150   This section mainly introduces our automatic fire-identification algorithm for producing NSMC-Himawari-8 fire product, based on original data obtained from Himawari-8/AHI.

3.1 Principle of fire-pixel identification

The basic principle of fire detection based on remote sensing mainly depends on two conditions: the increase of fire temperature leads to the enhancement of thermal radiation, and the difference in the growth range of radiation energy
155   between different thermal infrared bands (Csiszar et al., 2006). Different objects in nature have a diversity of spectral characteristics due to their special temperature and physical and chemical properties (Herold and Roberts, 2005). When biomass is burned, the main radiation sources are flame, carbides with higher temperature, water vapor, smoke and so forth (Zhang and Kondragunta, 2008). According to Stephen-Boltzmann formula (Quinn and Martin, 1985), notable variations of surface radiation is sensitive to the temperature, which means the heat sources can be detected based on radiance change.

$$J = \varepsilon\sigma T^4 \tag{1}$$

160   Where J is radiant emittance. ε is the radiant coefficient. If it is an absolutely black body, $\varepsilon = 1$. σ is Stefan-Boltzmann constant, $\sigma = 5.67\times10\text{-}8$ W·m^{-2}·K^{-4}. T is absolute temperature.

Wien's displacement formula shows that the brightness temperature is inversely proportional to the wavelength of the radiation center. With the increase of brightness temperature, the radiation wavelength becomes shorter (Kuenzer and Dech, 2013).

$$\lambda_{max} = \frac{b}{T} \tag{2}$$

165 Where λ_{max} is the peak wavelength of radiation (unit: m). b is the proportional constant, Wien displacement constant, and the value is 0.002897 m·K. T is the absolute temperature. Blackbody temperature T is inversely proportional to peak radiation wavelength λ_{max}, as the higher temperature can lead to the smaller peak radiation wavelength.

The peak wavelength of surface radiation within normal temperature is close to that at Band 13 and Band 14. When biomass is burned, the temperature can reach 750 K, and the radiation peak wavelength is close to Band 7 (Yang et al., 2017). Taking
170 the radiation when the surface features are not burning as the background radiation, the difference between the combustion radiation and the background radiation is notably in fire pixels, based on which the fire information can be extracted and analyzed. Band 7 of Himawari−8/AHI is mid-infrared, with a wavelength of 3.88 μm, while Band 13 is far-infrared, with a wavelength of 10.41 μm, and Band 14 is infrared split-window band, with a wavelength of 11.23 μm, respectively. For this research, we considered Band 7, Band 13 and Band 14 for fire-pixel extraction.
175 According to the observation characteristics of geostationary satellites and the unique types of regional underlying surface in China, the fire-identification algorithm for producing NSMC-Himawari-8 fire product has been further improved and
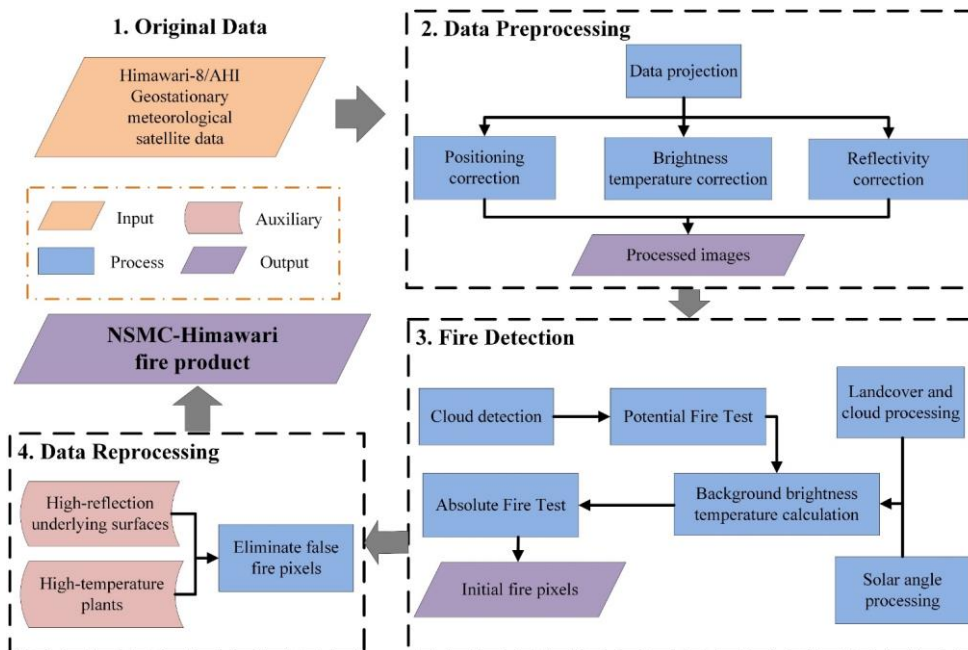
enhanced, from our FY-3D global fire-identification algorithm (Chen et al., 2022a). The major improvement of this fire-extraction algorithm, compared with previous algorithms, lies in the dynamic adjustment of fire-identification thresholds and the reprocessing of the heat source. The general steps for generating NSMC-Himawari fire product is briefly explained in Fig. 2, and the significant procedures are introduced as follows.
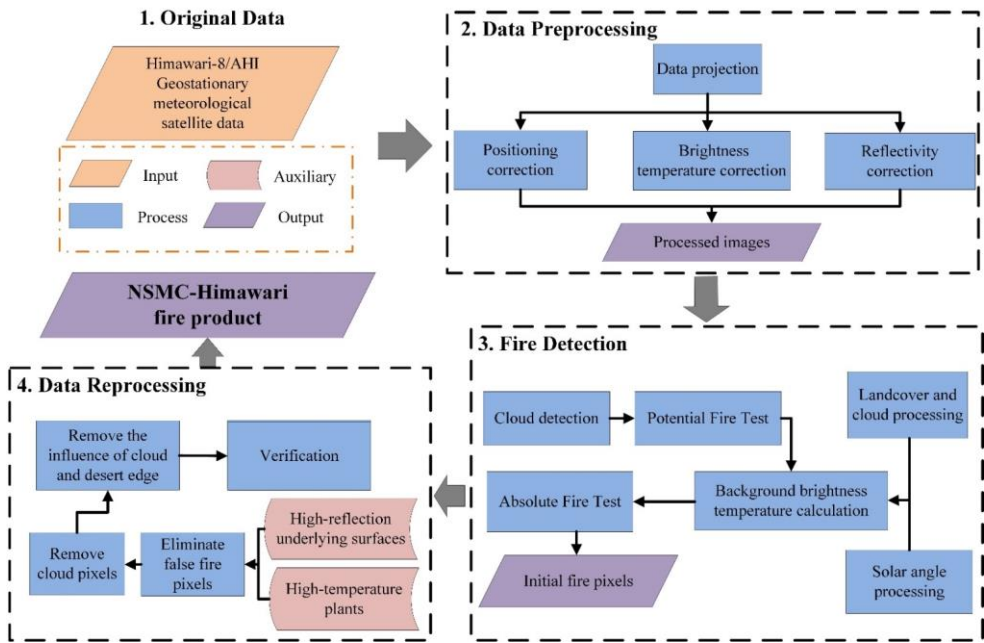
Figure 2: General flowchart for generating NSMC-Himawari fire products.

3.2 The fire-identification algorithm of NSMC- Himawari fire product

3.2.1 Detection of cloud pixels

185   The cloud coverage has a major impact on the confidence level of fire products (Schroeder et al., 2008). On one hand, the existence of cloud can easily block the ground fire information, causing omission and commission errors. On the other hand, the specular reflection of cloud may lead to the misjudgment of fire pixels (Arino et al., 2012). Therefore, cloud detection is an important step for effective identifying fire pixels. Wildfires in China are mainly concentrated in the Northeast, North, South and Southwest China, with differences across months (Cui et al., 2019).

190 According to the distinct geographical and climatic characteristics, the fire prevention period, which is decided by the State Forestry Administration in China, is mainly divided into autumn-winter and winter-spring. However, from June to September, the number of fire spots decreases significantly, owing to ample rainfall, higher humidity of combustible substance and wider cloud coverage.

To better present the influence of cloud, we displayed the FY-4A cloud coverage data in 2020, including 75000 cloud 195 images with a hit rate of approximately 92%, which is as accurate as Himawari-8 and matches MODIS by up to 67% (wang et al., 2019), to briefly demonstrate the spatial distribution of cloud coverage (as shown in Fig. 3). From May, the cloud coverage of the entire country gradually increased, and the cloud coverage in other areas except Sichuan Basin decreased from November to next February. Generally, under the same ground and observation conditions, the higher cloud coverage,
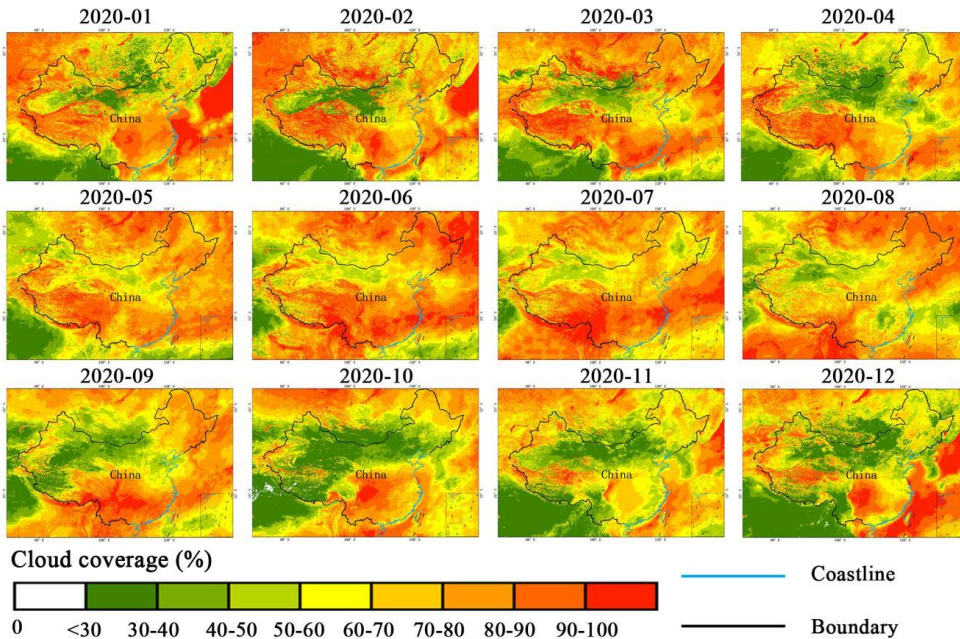
the less number of fire pixels identified by satellite.
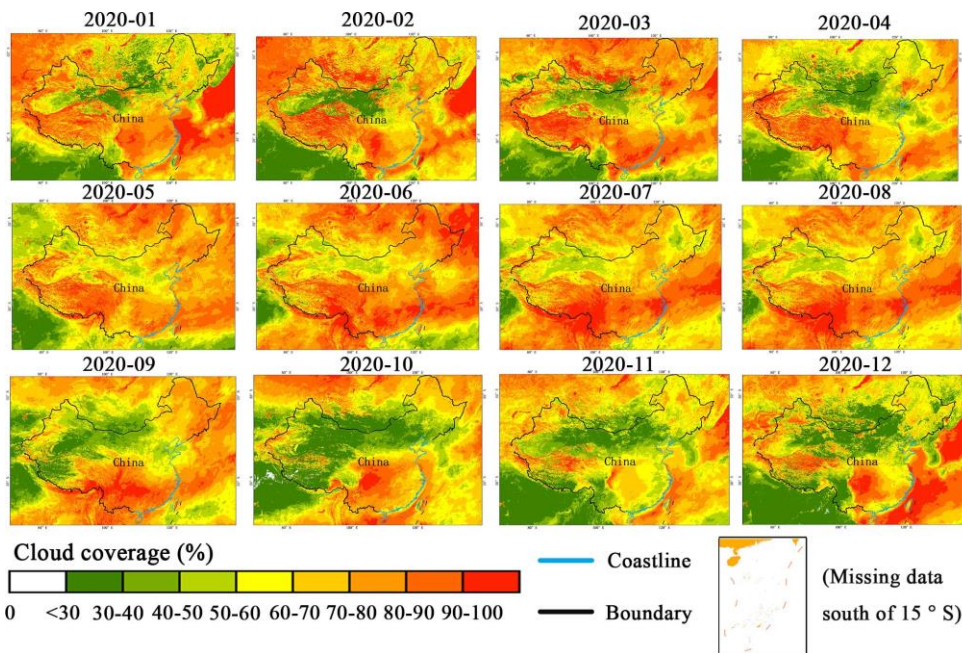
Figure 3: The spatial distribution of cloud coverage across China in 2020 (based on the Fengyun-4a satellite data).

The principle of cloud-identification for this research is similar to that of our previous FY-3D fire products (Chen et al., 2022a). According to the difference of brightness temperature and reflectivity between cloud and ground pixels, high-reflection characteristics of cloud pixels in visible-light bands and temperature characteristics in thermal infrared bands were employed for cloud removal. The observed pixels were then divided into cloud pixels and clear sky pixels in different spectral segments. According to the distribution characteristics of clouds in China, the reflectance difference among cloud, water and land pixels, and our previous product experience of the National Satellite Meteorological Center of China (Chen et al., 2022a, 2022b) we conducted multiple experiments and optimize the threshold value of the cloud-identification algorithm, and re differentiate the criteria. We classified cloud pixels according to the rules shown in Table 2. When the pixel meets any of the following conditions, it was identified as a cloud pixel.

Table 2. List of cloud pixel determinations.

Number	Conditions
1	$T_7 - T_{13} < 4$ K

2	$T_7 - T_{13} > 20\ K\ \&\ (T_7 < 275\ K\ |\ T_{13} < 270\ K)$
3	$R_{vis} > 0.28\ \&\ \theta_{sz} < 70°$
4	$T_{14} < 265\ K$
5	$T_{13} < 270\ K\ \&\ (T_{13}\text{-}T_{14} < 4\ K\ |\ T_{13}\text{-}T_{14} > 60\ K)$

T_7 is the brightness temperature at 3.9 µm~~mid-infrared~~ band; T_{13} is the brightness temperature at 10.4 µm ~~far-infrared~~ band; T_{14} is the brightness temperature at 11.2 µm~~far-infrared~~ band; R_{vis} is the reflectivity at visible light band; θ_{sz} is solar zenith angle. Note: these five rules are set to exclude a diversity of cloud biases and a pixel that meets any rule in Table 2.

3.2.2 Calculation of background temperature

As a generally accepted principle for fire detection, if there is a true fire spot in the observation pixel, the brightness temperature of the pixel at Band 7 and 14 is usually notably higher than the background brightness temperature. And the temperature difference at Band 7 is also higher than that at Band 14. In this case, the brightness temperature of background pixels is an important physical index for automatic fire-identification in our research. As the background temperature cannot be obtained from the fire pixels, it should be calculated according to the average of their surrounding pixels. However, if the average brightness temperature of surrounding pixels selected is excessively high, there may be massive omission errors in fire detection. Conversely, if the average of surrounding pixels selected is lower than normal background brightness temperature, a great number of commission errors may be generated. Therefore, appropriate selection of surrounding pixels is essential for calculating brightness temperature of background pixels. When calculating the background brightness temperature, pixels that may contain fire pixels, water pixels, cloudy pixels and other pixels influenced by solar flare, with excessively low and high brightness temperature, should be regarded as invalid pixels and removed before background temperature calculation.

According to repeated experiments, based on the windowing method, we selected TOP 20 % high temperature pixels in the initial window area (7 × 7) as the suspected high-temperature, and further identified and eliminated them gradually. The suspicious high-temperature pixels can successively be determined, if their brightness temperature at Band 7 meets the following equation:

$$T_7 \geq T_{13} + 100 \times R_{vis} + 20K \tag{3}$$

Where T_7 is the brightness temperature of the suspicious high-temperature pixel at Band 7. T_{13} is the brightness temperature of suspicious high-temperature pixel at Band 13. R_{vis} is the reflectivity value of suspicious high-temperature pixel in the visible light band.

After we removed the above mentioned disturbing pixels in the window area, we calculated the background temperature based on the remained effective background pixels around the candidate fire pixel. Specifically, the background brightness

temperature, the averaged brightness temperature of the effective background pixels at Band 7 in the window area, could be calculated through the following method.

$$T_{7\_bg} = (\sum_{i=1}^{n} T_{7i})/n \qquad (4)$$

Where T_{7_bg} is the averaged brightness temperature of effective background pixels at Band 7 the in window area, which represents the background brightness temperature. T_{7i} is brightness temperature of effective background pixels at Band 7. n is the number of effective background pixels.

Under clear sky conditions, the satellite could better monitor the fire information on the underlying surface, and the window size was set to 7×7 pixels as initial window area. If the number of available monitored pixels in the window was less than 20 % of the total pixels in the neighborhood due to cloud cover and other factors, then the 7×7 window was extended to 9×9, 11×11 and 19×19. If it remained not applicable, these candidate fire pixels were directly marked as non-fire pixels.

3.2.3 The identification of fire pixels

The geostationary meteorological satellite can access 24-hour observation. Since the monitored fire characteristics are changeable, it is necessary to dynamically adjust the identification threshold considering the influence of various factors. The main factors include the solar altitude angle, cloud surface and the zone bare of vegetation, which have a great impact on the discrimination accuracy. For instance, the solar altitude angle affects the brightness temperature of the detection area. The solar altitude angle of each detection area increases from 0° to the maximum angle with time, and then decrease to 0°. The solar radiation intensity received by the surface increases with the increase of solar altitude angle, and the increment of brightness temperature is different in different regions. If we employ a fixed identification-threshold in all different regions in China, it inevitably causes a large number of omission and commission errors. At the same time, the capability of non-vegetation areas to absorb solar radiation is stronger than that of vegetation, and the difference of brightness temperature between such non-vegetation pixels and surrounding pixels is significant. Therefore, to increase the accuracy of fire detection, it is essential to dynamically adjust background coefficients according to solar altitude angle, cloud coverage and non-vegetation pixels. Based on the review of historical fire records, we set the identification thresholds and correction coefficients, which varied across monitoring time and observation areas. According to the following condition-check (absolute and relative conditions), fire pixels could be effectively extracted. When the following conditions are met, a pixel can be identified as a fire pixel:

$$T_7 > 360K \text{ and } R_{vis} < 0.7 \text{ and } \theta_{sz} > 87° \qquad (5)$$

$$T_7 \geq T_{7\_bg} + a(P_v, P_c, \theta_{sz}) \times \delta T_{7\_bg} \text{ and } T_{7\_13} \geq T_{7\_13bg} + a(P_v, P_c, \theta_{sz}) \times \delta T_{7\_13\_bg} \qquad (6)$$

Where T_7 is the brightness temperature of the candidate pixel at Band 7. R_{vis} is the reflectivity of the identified pixel at the visible-light band. θ_{sz} is solar zenith angle. T_{7_bg} is the background brightness temperature. T_{7_13} is the difference of brightness temperature between Band 7 and Band 13. $T_{7\_13\_bg}$ is the difference of background brightness temperature between Band 7 and Band 13. This condition is set to identify the difference under a variety of underlying surfaces in the window. δT_{7_bg} is the standard deviation of the brightness temperature of background pixels. $\delta T_{7\_13\_bg}$ is the difference of the standard deviation of background brightness temperature between Band 7 and Band 13.

The specific calculation method of the standard deviation is as follows :

$$\delta T_{7\_bg} = \sqrt{\sum_{i=1}^{n} (T_{7i} - T_{7\_bg})^2 / n} \qquad (7)$$

$$\delta T_{7\_13\_bg} = \sqrt{\sum_{i=1}^{n} (T_{7\_13i} - T_{7\_13\_bg})^2 / n} \qquad (8)$$

Where n is the number of effective background pixels in the window. T_{7i} is brightness temperature of effective background pixels at Band 7. T_{7_13i} is the difference of brightness temperature of effective background pixels between Band 7 and Band 13. When the land cover types in the window are generally consistent, $\delta T_{7\_13\_bg}$ is relatively small. For the candidate fire pixels, when $\delta T_{7\_13\_bg}$ is smaller than 2 K, the value is set to 2 K. When $\delta T_{7\_13\_bg}$ is large than 4 K, the value is replaced by 4 K.

In the identification algorithm, $a(P_v, P_c, \theta_{sz})$ is a coefficient function, which is related to the non-vegetation pixel ratio, cloud pixel ratio and solar zenith angle. The coefficient varies with different monitoring areas, detection time and angles. Therefore, the identification threshold can be dynamically adjusted according to different situations. The calculation method is as follows:

$$a(P_v, P_c, \theta_{sz}) = \begin{cases} (sin\theta_{sz} + 1) \times (1 + P_v) \times (1 + P_c); & \theta_{sz} < 60° \\ (1.2 * sin\theta_{sz} + 1) \times (1 + P_v) \times (1 + P_c)^2; & \theta_{sz} \geq 60° \end{cases} \qquad (9)$$

Where P_v is the proportion of non-vegetation pixels in window. θ_{sz} is the solar altitude angle of the identified pixel. $a(P_v, P_c, \theta_{sz})$ increases with θ_{sz} and P_v to reduce the false errors generated by the solar reflection signal. P_c is the proportion of cloud pixels in window area, and the use of P_c can reduce the false identification of fire pixels at the edge of clouds. The identification threshold increases with P_c.

3.3 Reprocessing of the fire production

The thermal anomalies signal at the mid-infrared band (Band 7), also includes non-fire heat source information, e.g. the thermal signals caused by cloud edge, high reflection underlying surface, bare ground, artificial buildings, factories and other non-fire heat sources. Therefore, the preliminarily extracted heat sources should be reprocessed to eliminate false fire pixels.

3.3.1 The removal of cloud pixels

If extracted high-temperature pixels meet following conditions, it is considered to be affected by cloud and should not be regarded as fire pixels.

$$R_{vis} \geq R_{vis_{bg}} + R_{c\_th} \ \& \ T_{13} \leq T_{13\_bg} - T_{c\_th} \tag{10}$$

Which R_{c_th} is the discrimination threshold of cloud influence at the visible light, and the initial value is set to 0.15. T_{c_th} is the discrimination threshold for cloud interference at Band 13, and the initial value is set to 5 K. $\underline{R_{vis} \text{ is the reflectivity of the high-temperature pixel at the visible-light band.} R_{vis_{bg}} \text{ is the averaged reflectivity of effective background pixels in the window at the visible-light band.}}$ ~~Rvis is the reflectivity value of the high-temperature pixel at the visible-light band.~~ $R_{vis_{bg}}$ ~~is the reflectivity of the high-temperature pixel at the visible-light band.~~ T_{13} is the brightness temperature of the high-temperature pixel at Band 13. T_{13_bg} is the averaged brightness temperature of effective background pixels in the window at Band 13.

3.3.2 The removal of the influence of cloud and desert edge

When the pixel is at the edge of the cloud, the brightness temperature of the mixed pixel with a few cloud is lower, as the cloud temperature is lower than the surface temperature. When calculating the brightness temperature and standard deviation of background pixels, the mixed pixels are still employed as effective pixels, thus reducing the background brightness temperature and affecting standard deviation. Although cloud pixels have been removed through previous steps, the impact of mixed pixels remains. Based on years of operation and maintenance experience of the National Satellite Meteorological Center, we have made the following amendments. If the high-temperature pixel meets the following conditions, it is considered to be influenced by cloud and desert edge and not regarded as a fire pixel.

$$T_7 \leq T_{7\_bg} + C \times \delta T_{7\_bg} \ \& \ T_{7\_13} \leq T_{7\_13\_bg} + C \times \delta T_{7\_13\_bg} \tag{11}$$

C is the recognition threshold of cloud edge and desert edge, and the initial value is set to 8. T_{7_13} is the difference of the brightness temperature between Band 7 and Band 13. $T_{7\_13\_bg}$ is the difference of background brightness temperature between Band 7 and Band 13. $\delta T_{7\_13\_bg}$ is the difference of standard deviation of background brightness temperature between Band 7 and Band 13.

3.3.3 The removal of high-reflection underlying surfaces and high-temperature plants

High-temperature factories and high-reflection underlying surfaces are the main ground interference factors affecting the accuracy of satellite-based fire detection. Due to the large amount of thermal radiation generated in the production process, high-temperature factories present similar characteristics to real fire spots at the mid infrared band. For satellite-based fire detection, although these interference sources, which may easily be recognized as false fires, are well known, currently employed fire products rarely exclude these basic thermal anomalies, causing a large uncertain to the product accuracy.

To effectively remove potential false fires and improve the reliability of the Himawari-8 fire products in China, National Satellite Meteorological Centre and State Grid cooperated to generate a data base concerning major high-temperature plants and high-reflection underlying surfaces in China through AI-assisted visual interpretation based on the comprehensive integration of multiple remote sensing sources, including NOAA-20/VIIRS (https://lpdaac.usgs.gov/products/), NPP/VIIRS (https://psl.noaa.gov/data/), TERRA/MODIS and AUQA/MODIS (https://ladsweb.modaps.eosdis.nasa.gov/). The specific parameters of these sources are shown in Table 3.

Table 3. Main parameters of employed data sources for AI-assisted extraction of heating-sources.

Satellite	Sensor	Bands	Resolution (m)
NOAA-20		I1 - I5 and M13	375
NPP	VIIRS	M5、M7、M11、M13、M15、M16	750
TERRA AUQA	MODIS	Band 20 - 36	1000

The specific procedure for extracting these surface thermal sources is briefly introduced as follows: for interference sources that can generate strong quantity of heat, such as steel plants, thermal plants and chemical plants, we mainly conducted extraction through visual interpretation. The thermal anomalies detected based on NOAA-20, NPP and other remote sensing sources were matched to Google Maps and further confirmed with high-resolution images. In this case, we identified more than 7000 thermal interference polygons and added to the database.

Since the observation angle of the geostationary meteorological satellite is fixed, the impact of ground mirror reflection on the observation instrument is a common cause for falsely detected fires. Specifically, large photovoltaic panels in photovoltaic power plants, which are wildly distributed, are the major sources influencing the extraction of actual fires. Firstly, we manually extracted a large number of photovoltaic panel images from the Google satellite images, and employed them as a sample to conduct sample training through deep learning, based on which an extraction model was established; Secondly, we employed an image segmentation-classification model (Yuan et al., 2013) to conduct a large-scale extraction of photovoltaic panels in China, and established a primary sample library of photovoltaic panel. Thirdly, massive manually

editing was conducted to maximally reduce the classification errors. Successively, part of the manual identification results were added to the training samples to further improve the model accuracy. Based on this strategy, we classified more than 9900 photovoltaic panel pixels. The minimum area of extracted photovoltaic panels was dozens of square meters, and the maximum was dozens of square kilometers (as shown is Fig. 4).

335
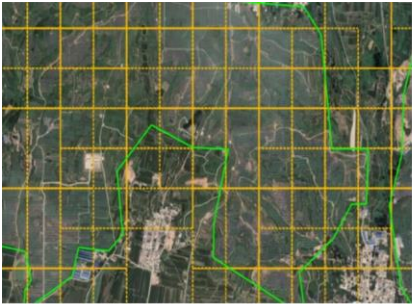
(a) Mountain   (b) Plain

(c) Water   (d) Roof
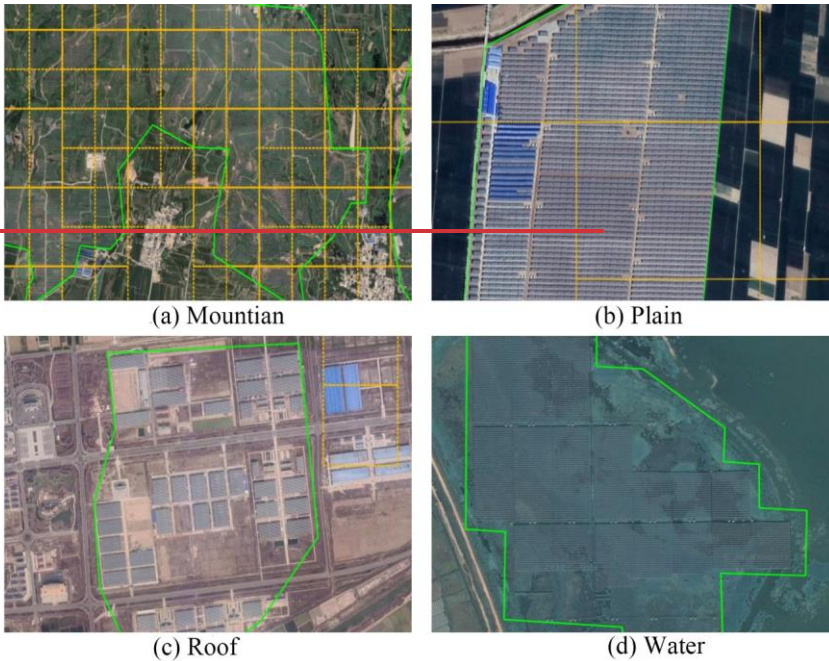
Figure 4: Samples of extracted photovoltaic panels (aerial images from © Google Maps).

340   Based on accuracy assessment, the primary accuracy of AI recognition is about 87 %. With the following manual editing, the overall accuracy of the extracted thermal sources and photovoltaic panels exceeded 95 %. This dataset of high-temperature plants and high-reflection underlying surfaces (as shown in Fig. 5) has been updated annually by China Meteorological Administration and State Grid. By comparing pre-selected fire pixels and this data set, we removed a majority of false fire pixels and largely enhanced the accuracy of our NSMC-Himawari-8 fire product.
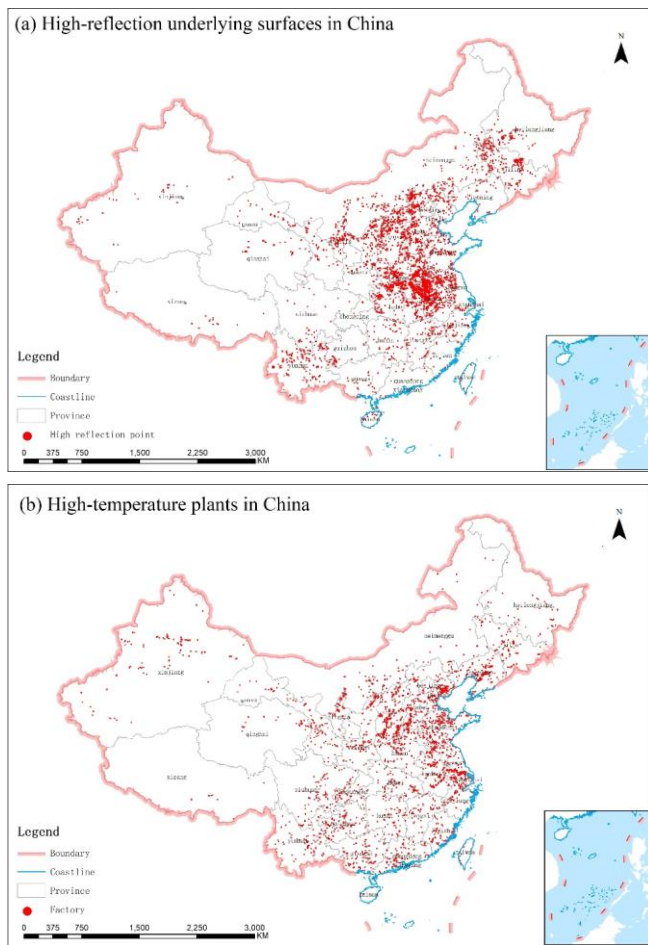
Figure 5: The high-temperature plants and high-reflection underlying surfaces identified in China for 2021.

3.4 Verification

Our NSMC-Himawari-8 fire product was evaluated using the JMA-Himawari-8 fire products and on-site collected reference of true fires. Specifically, the evaluation was conducted in the following steps. Firstly, through excessive manual verification,

we compared the number of ground interference sources (high-temperature plants and high-reflection underlying surfaces), which are the main source of falsely detected fire pixels, included in the JMA-Himawari-8 and NSMC-Himawari-8 fire products. Secondly,we examined the consistency of NSMC-Himawari-8 and JMA-Himawari-8 fire product in China from the perspective of the total number of fire pixels, different underlying surfaces and different brightness temperatures. Finally,we employed a rare dataset of on-site collected burning records, which was jointly established by the State Grid and China Meteorological Administration throughout 2021 in five provinces (Guangdong, Guangxi, Yunnan, Guizhou and Hainan) in China, as reference data to evaluate the overall accuracy of NSMC-Himawari-8 fire products in China.

4 Result

4.1 Accuracy assessment of JMA-Himawari-8 and NSMC-Himawari-8 fire products in terms of falsely identified interference sources

Based on the original hourly Himawari-8 data from 2019 to 2021, we produced NSMC-Himawari-8 fire product through above introduced fire-extraction approach. Through excessive manual one-by-one-pixel check, we compared the number of interference sources misidentified in the JMA-Himawari-8 and NSMC-Himawari-8 fire product.

As shown in Fig 6 (a), the number of misidentified fire pixels in JMA-Himawari-8 product, majorly caused by ground thermal sources, is much larger than NSMC-Himawari-8 product in all months. The monthly misidentified fire pixels for JMA - Himawari-8 fire product was on average 13000, ranging from 5000 to 20000 in different months, making the number of hourly misidentified fire pixels close to 18. As a comparison, the monthly misidentified fire pixels for NSMC-Himawari-8 fire product was on average less than 1500, ranging from 200 to 4500 in different months, making the number of hourly misidentified fire pixels close to 2.

To further present the influence of interference sources in the two products, we also calculated the ratio of monthly true fire pixels to misidentified pixels. As shown in Fig. 6 (b), except from June to September, the true/misidentified ratio for NSMC-Himawari-8 fire product is notably higher than that of JMA. The largest ratio value 58 appeared in April that is, there was only one interference source in every 59 identified pixels. From May to September, due to the relatively small number of real fire pixels, the true/misidentified ratio for both products was smaller than 10, with a minimum value close to 1:1 in August, suggesting the influence of interference sources was extremely strong influence in less-fire seasons.
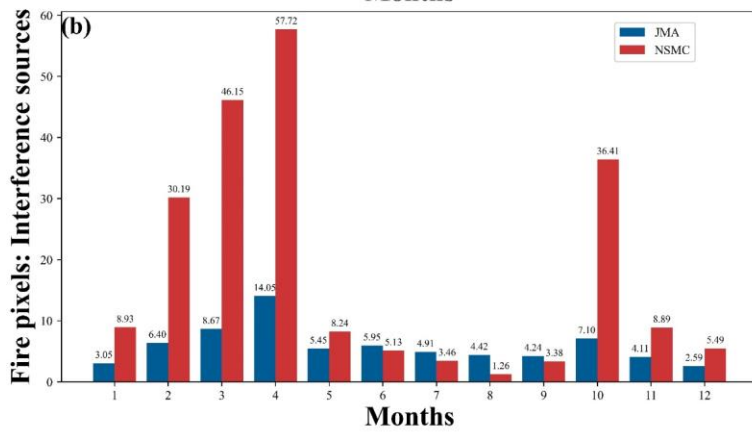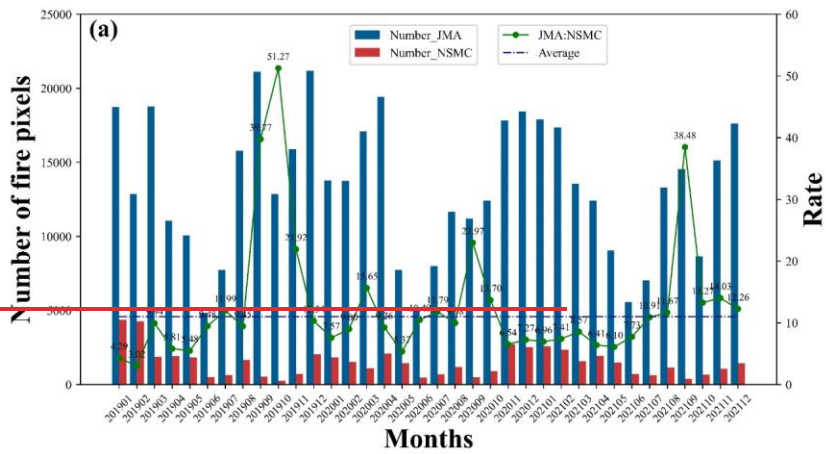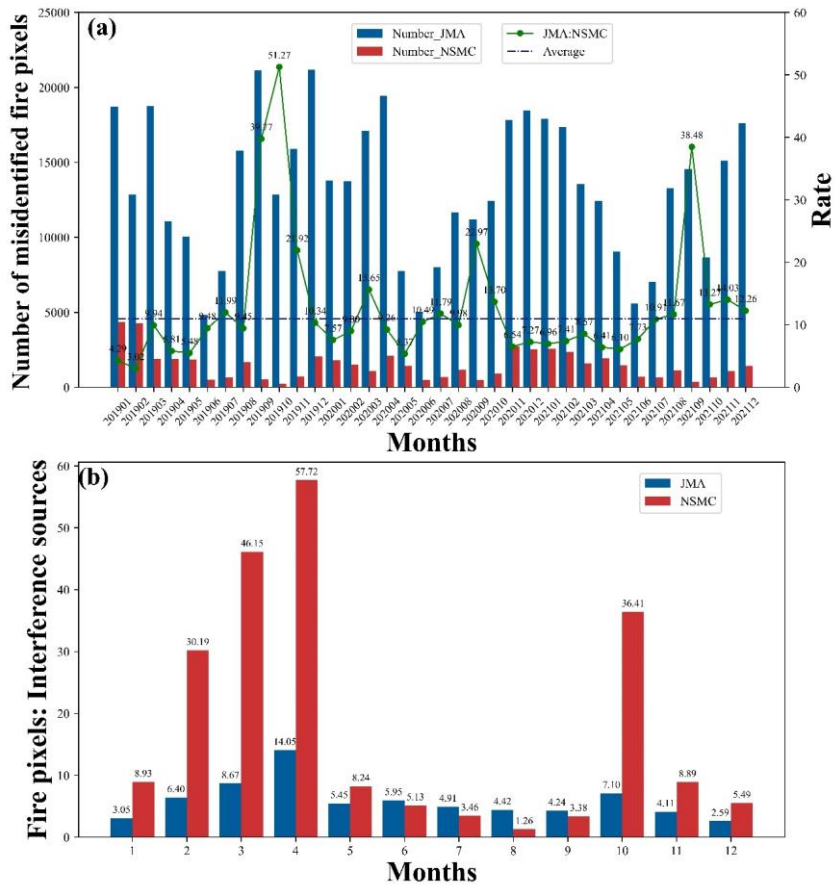
Figure 6: The influence of interference sources in JMA-Himawari and NSMC-Himawari fire products across months. (a) The total number of misidentified fire pixels. (b) The average ratio of true to misclassified fire pixels.

375

4.2 Consistency between JMA-Himawari-8 and NSMC-Himawari-8 fire product

In addition to accuracy assessment in terms of misidentified fire pixels, we also examined the consistence between JMA-Himawari-8 and NSMC-Himawari-8 fire product in terms of the number of fire pixels, underlying surfaces and brightness temperature.

4.2.1 Consistency in terms of the total number of fire pixels

From January 2019 to December 2021, there were totally 1,136,119 fire pixels identified in NSMC-Himawari-8 fire product while there were 3,232,940 fire pixels identified in JMA-Himawari-8 fire product. The total number of identified fire pixels from JMA-Himawari-8 fire product was around three times of that of NSMC-Himawari-8 fire product. As introduced above, the large difference was majorly attributed to the fact that NSMC-Himawari fire product avoided a majority of ground interference thermal sources.
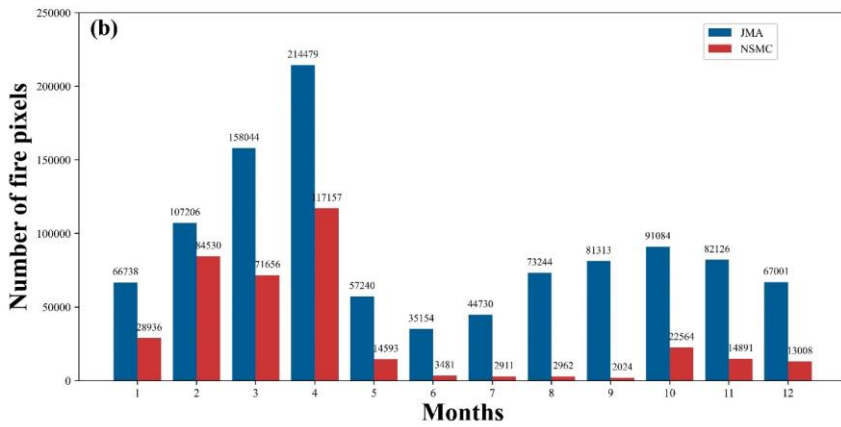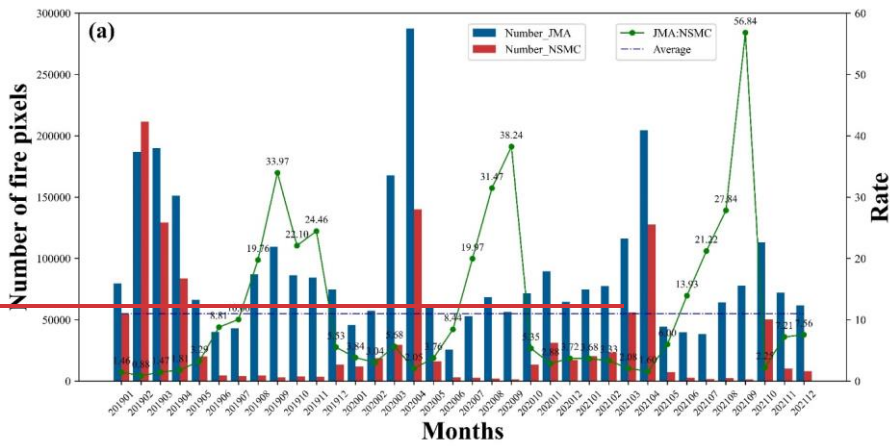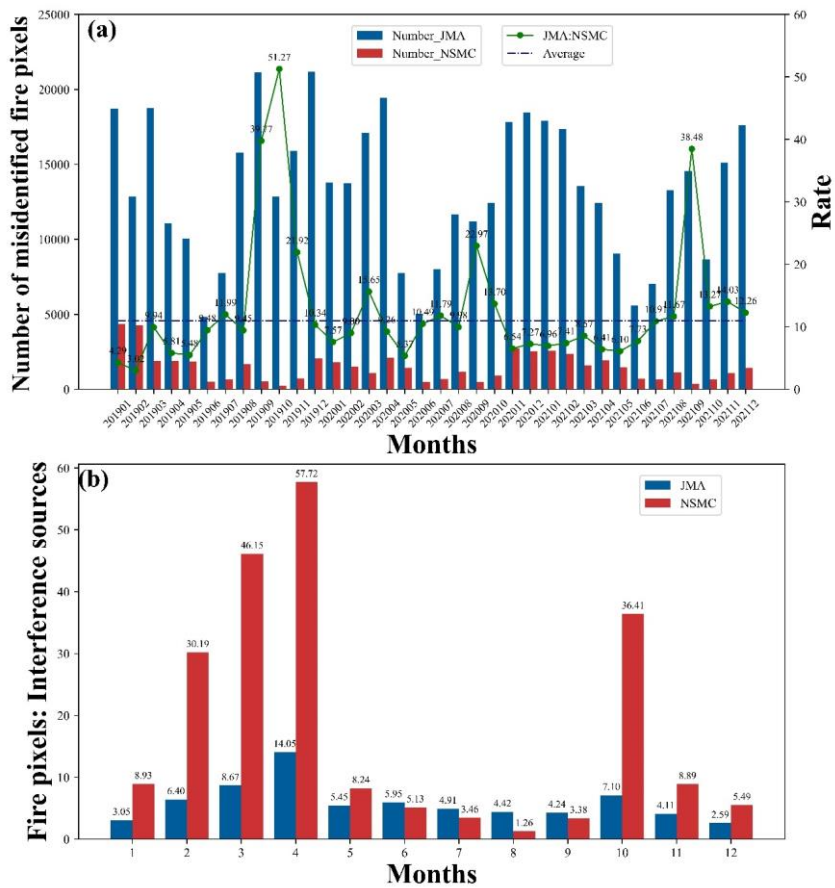
390**Figure 7: The total number of identified fire pixels in two fire products. (a) Time series. (b) Monthly average.**

At the monthly basis (Fig. 7), For NSMC-Himawari-8 fire product, identified fire pixels majorly concentrated from January to April while the number of fire pixels was small from June to September every year. As a comparison, for JMA-Himawari-8 fire product, in addition to the period from January to April, there was another peak fire season from June to September. The number of identified fire pixels in JMA-Himawari-8 product was on average ten times of that of NSMC-Himawari-8 fire product from June to September, which is actually a season with a relatively small number of forest fires and crop-residue

burning. This strong inconsistence further proved the importance of removal of potential interference fire pixels and the reliability of NSMC-Himawari-8 fire product, especially in the less-fire seasons.

We further examined the overall consistence between JMA-Himawari-8 and NSMC-Himawari-8 fire products from two different perspectives. From the JMA perspective, we mainly checked the average possibility of one identified fire pixel in JMA-Himawari-8 fire product also included in the NSMC-Himawari-8 fire product. From the NSMC perspective, we mainly checked the average possibility of one identified fire pixel also included in the JMA-Himawari-8 fire product.

As shown in Fig. 8, the consistency was relatively low from the period from June to September, and much higher from the period from January to April. The consistence from the NSMC perspective, ranging from 42 % to 87 % across months, was much higher than the consistence from the JMA perspective, ranging from 1 % to 62 %. This is majorly attributed to the large amount of false fire pixels included in the JMA perspective have been removed in NSMC-Himawari-8 fire product, and thus the possibility of finding a counterpart was largely reduced. Meanwhile, JMA-Himawari-8 fire product retained a majority of effective true fire pixels in the original Himawari-8 files and thus the possibility of finding a counterpart in JMA-Himawari-8 fire product was relatively large. The consistence check further proved that NSMC-Himawari-8 fire product effectively maintained useful information from original Himawari-8 sources and presented a largely enhanced reliability.
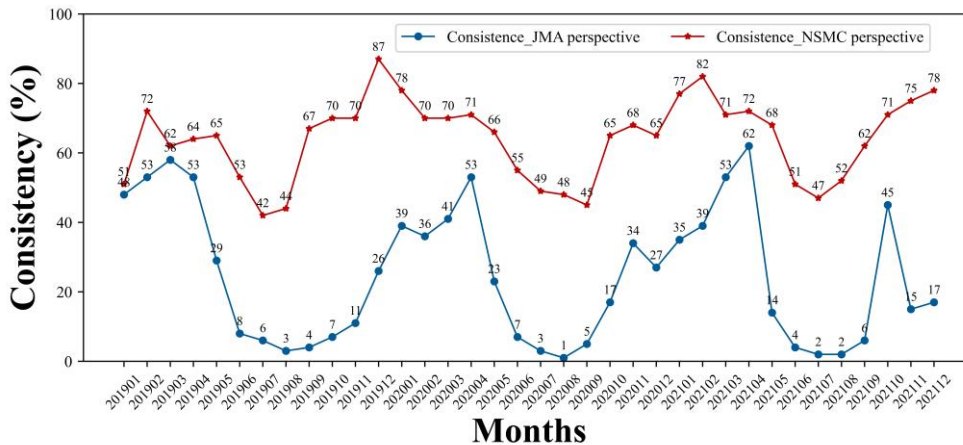
Figure 8: The general consistency between JMA-Himawari-8 and NSMC-Himawari-8 fire product across months.

4.2.2 Consistency on different underlying surfaces

China has a vast territory and a diversity of underlying surfaces, leading to large variations of fire types and difficulty of fire detection across regions. Specifically, compared with southern forest wildfires that could generally burn very large areas and

last several months, fires in the Northeast of China are majorly small-sized fires that burn in relatively low intensity in agriculture and forestry lands. According to Climate Change Initiative (CCI) Land Cover V2 (http://maps.elie.ucl.ac.be/CCI/viewer/download.php), with a spatial resolution of 300 m in 2015, We divided the underlying surfaces into Built-up areas, Farmland (straw), Grass (grassland) and Forest, respectively.
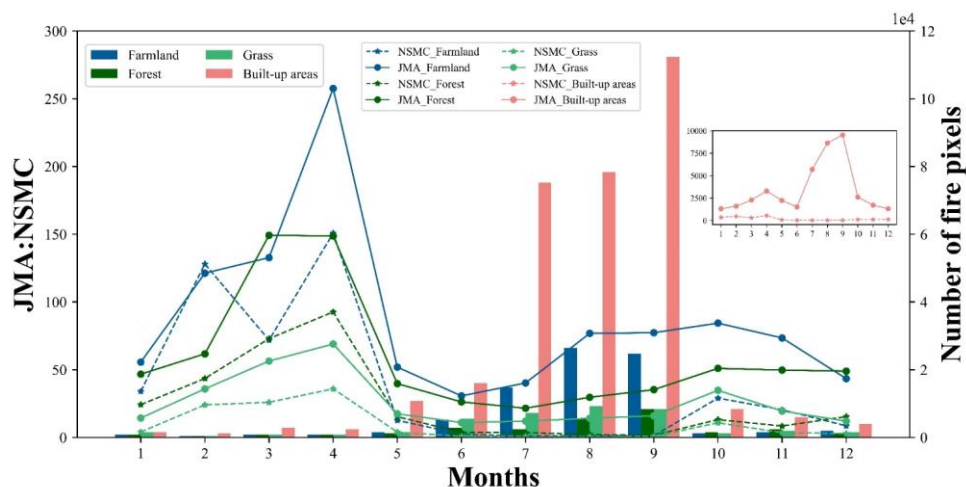
Figure 9: The number of fire pixels and ratio between JMA and NSMC fire products under different underlying surfaces across months.

Figure 9 shows the monthly average of fire pixels identified on different underlying surfaces from 2019 to 2021. The total number of fire pixels in farmland was the largest for both fire products, followed by forest, and the general trend of the two fire products was similar in number. Generally, as Table 4 shown, the consistence between two products from NSMC perspective was relatively high for all underlying surfaces, with an average consistence larger than 70 %. As a comparison, from JMA perspective, the consistence between two products was relatively low for all underlying surface types. Figure 9 also suggested that the number of fire pixels identified on building areas in JMA-Himawari-8 fire product during June to September was more-than-100 times of that identified in NSMC-Himawari-8 fire product. Given that there is actually a very limited number of fires occurred on buildings during this period, it is highly possible the excessive number of fire pixels detected on building areas in JMA-Himawari-8 fire product resulted from false alarms caused by ground thermal sources. Meanwhile, the maximally reduced fire-pixels identified on building pixels additionally proved the advantage of employing our ground-thermal-source database to remove false alarms.

Table 4. The consistence between JMA and NSMC-Himawari-8 fire product under different underlying surfaces.

	Jan (%)	Feb (%)	Mar (%)	Apr (%)	May (%)	Jun (%)	Jul (%)	Aug (%)	Sep (%)	Oct (%)	Nov (%)	Dec (%)
NSMC_Farmland	63.50	64.43	62.18	68.75	63.64	55.51	45.20	48.60	64.30	71.31	67.07	70.27
JMA_Farmland	42.06	48.54	40.68	55.78	19.16	5.10	1.84	0.87	1.43	25.09	21.43	18.14
NSMC_Forest	73.58	74.43	74.51	70.17	70.69	57.76	49.98	51.92	65.12	70.56	79.54	81.38
JMA_Forest	47.51	53.37	51.62	60.68	32.85	10.07	10.06	4.51	4.17	22.10	18.87	35.96
NSMC_Grass	69.10	67.44	63.04	64.22	60.99	39.41	38.42	44.66	64.42	67.14	67.18	71.67
JMA_Grass	28.62	45.90	38.91	52.51	17.97	3.22	2.97	2.50	4.54	25.48	14.14	23.77
NSMC_Built_up areas	79.47	71.02	73.02	67.50	68.11	63.89	51.62	47.65	73.33	78.14	83.81	90.03
JMA_Built_up areas	15.23	14.76	8.11	14.10	2.96	1.10	0.35	0.21	0.23	5.42	4.31	4.77

4.2.3 Consistency under different brightness temperature

The key to extract fire pixels is to precisely obtain their brightness temperature and set fire-extraction thresholds accordingly. Consequently, the brightness temperature of identified fire pixels has a notable influence on the consistence between JMA-Himawari-8 and NSMC-Himawari-8 fire product.

As shown in Fig. 10, the higher the brightness temperature, the higher consistence was. When the brightness temperature is less than 270 K, the consistency between the two fire products was less than 20 %, and the consistency increased rapidly with the rise of the brightness temperature. When the brightness temperature exceeded 330 K, the consistency between two products exceeded 70%. It is noted here that the brightness temperature for a fire pixel was not solely decided by the temperature of fires. Since a occurring fire sometimes simply occupied a very small percentage of a 2 km × 2 km cell, then the brightness temperature for this pixel was majorly decided by the background brightness temperature. When the brightness temperature was extremely high (e.g. over 330 K) and exceeded normal background temperature, this pixel was most likely a true fire spot, which thus was included by both the JMA-Himawari-8 and NSMC-Himawari-8 fire product. When the brightness temperature of one pixel was relatively low (e.g. around 270 K), yet much higher than its surrounding pixels, it may also be considered as fire pixel. This phenomenon is common for fire detection in northern China in winter. However, the existence of ground thermal sources can lead to the misidentification of fire pixels. Since we employed the dataset of ground interference sources, a large amount of misidentified fire pixels under low-temperature scenario, which are included in JMA-Himawari-8 fire product, has been removed from NSMC-Himawari-8 fire product, leading to a very small

450 consistence when the brightness temperature of target pixels was low. This output further revealed the strong influence of ground thermal sources on the reliance of extracted fire pixels.
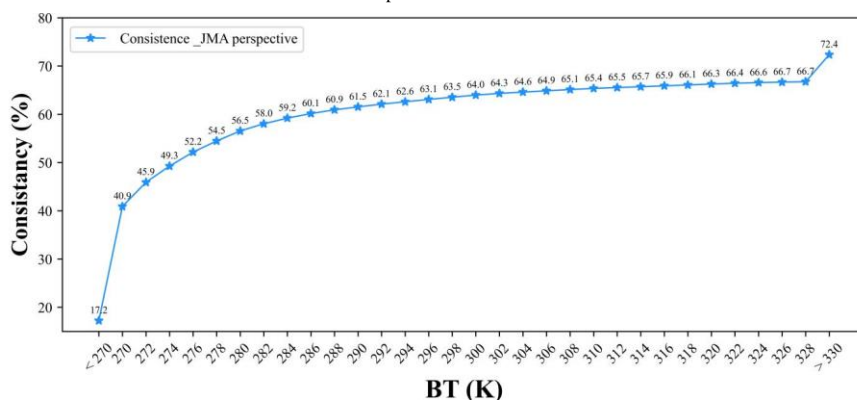
Figure 10: The variation of consistence between JMA-Himawari-8 and NSMC-Himawari-8 fire product under different brightness temperature.

455 **4.3 Accuracy assessment based on ground truth data**

Since the occurrence of wild fires is highly unpredictable and the duration of fires may be short, the real-time capture and continuous monitoring remains highly difficult. Therefore, the major challenge for verifying fire products lies in the lack of ground truth reference, and the reliability of JMA-Himawari-8 fire product in China remains unknown.

To obtain reliable and large scale reference for fire-detection, STATE GRID Corporation of China and China Meteorological
460 Administration jointly conducted annual fire-detection experiment since 2017 in five provinces Guangdong, Guangxi, Yunnan, Guizhou and Hainan in China. Massive drones have been employed to check the occurrence of fires and report the location and occurring time of actual fires. For this research, we employed field-collected fire reference in the five provinces throughout 2021 for accuracy assessment. By comparing the actual information of fires and the corresponding information in the two products, we could obtained the omission, commission errors and overall accuracy of JMA-Himawari-8 and NSMC-
465 Himawari-8 fire products.

As shown in Table 5 and Fig. 11, there were a proportion of omission errors in both fire products. This type of errors was majorly caused by the limitation of sensors that some small fires within the 2km × 2km grid cannot be identified. Thanks to the dynamic fire-extraction thresholds adapted to China's local parameters, the number of fire-pixels correctly recognized by NSMC-Himawari-8 fire product (2174) was notably larger than that of JMA-Himawari-8 fire product (1648). Meanwhile,
470 the number of commission errors, which standard for those non-fire pixels misidentified as fire pixels, included in JMA-Himawari-8 fire product (1160) was much larger than that in NSMC-Himawari-8 fire product (413).

Table 5. Accuracy assessment of JMA-Himawari-8 and NSMC-Himawari-8 fire products based on field ground truth.

	Correct	Omission errors	Commission errors	Accuracy(%)	Accuracy without omission (%)
JMA	1648	243	1160	54	59
NSMC	2174	137	413	80	84

This is majorly attributed to our reprocessing of the preliminarily extracted fire pixels according to our data base of ground thermal sources, which removed a majority of false fire pixels. Disturbed by a large proportion of misidentified fire pixels, the overall accuracy of JMA-Himawari-8 fire product across China was simply 54 %. Even if we ignore those omission errors caused by sensor limitations, the overall accuracy was below 60 %. Therefore, the existing JMA-Himawari-8 fire product cannot provide reliable hourly monitoring of wildfires across China.
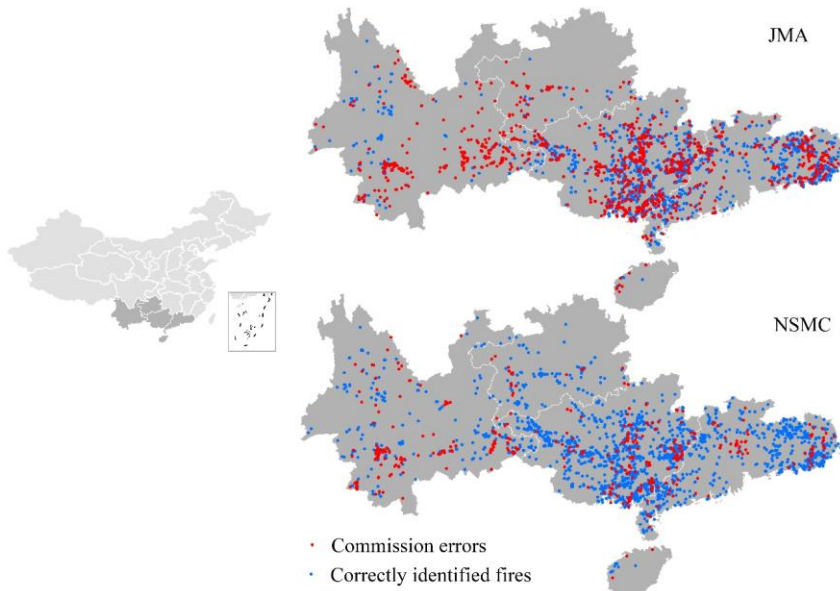
Figure 11: Accuracy assessment of NSMC-Himawari-8 and JMA-Himawari-8 fire products in China based on the ground-truth data.

As a comparison, with a notably improved number of correctly identified fire pixels and a significantly reduced number of misidentified fire pixels, the overall accuracy of NSMC-Himawari-8 fire product reached 80 %. If the omission errors were

not considered, the overall accuracy of NSMC-Himawari-8 fire product could further reach 84 %. The largely improved accuracy makes our fire product an ideal source for real-time fire monitoring in China.

5 Discussion

We compared the accuracy of JMA-Himawari-8 and NSMC-Himawari-8 fire products in China. Based on the field-collected evidence, NSMC-Himawari-8 fire products achieved a notably improved accuracy. This was mainly attributed to the additional consideration of underlying surface conditions, which effectively removed a large proportion of false fires. This result was consistent with the overall accuracy of our previous fire products. By comprehensively consider the underlying surfaces in China, FY-3D global fire product achieved a high consistence with the mainstream and most commonly employed MODIS fire product at the global scale and significantly improved accuracy in China (Chen et al., 2022). These results suggested that the accuracy of fire products was largely biased by the heating-sources, which cannot be easily avoided through previously set fire-detection thresholds, and additional data sources should be employed for removing this type of major noises. Despite a notably improved accuracy, limitations remains. Firstly, regardless the setting of major fire-detection parameters, the moderate spatial resolution of NSMC-Himawari-8 fire products (2 km) restricted its capability for identifying the occurrence of those small fires. To address this issue, the comprehensive consideration of NSMC-Himawari-8 fire products and other high resolution fire products (e.g. VIIRS fire products) may be a potential solution. Nevertheless, the reliability of these complementary fire products in China requires further verification and improvement. Secondly, during the early-morning and evening, due to the relatively low solar altitude, the identification of cloud removal was slightly influenced during this period. Thirdly, due to the vast coverage, the conditions of underlying surface varies significantly in China. Therefore, the setting of fire-identification thresholds may achieve different effects across regions. For those regions with complicated underlying surfaces, the reliability of NSMC-Himawari-8 fire products may be lower than the overall accuracy.

In recent years, there is a growing need for timely monitoring the occurrence of wild fires in China, especially for the identifying grassland fires and forest fires, which cause severe threat to public health and environment, and detecting human-induced crop-residue burning, which has become one major source for airborne pollutants. However, existing mainstream fire products cannot fully support these needs. The MODIS and FY-3D daily global fire products can solely visit the target area once per day. Meanwhile, JMA-Himawari-8 hourly fire products have the potential to provide quick-identification of wildfires. However, even without quantitative accuracy assessment, previous implementation conducted by major institutions (e.g. National State GRID and China Meteorological Administration) reported that JMA-Himawari-8 products presented large uncertainties across China. Therefore, JMA-Himawari-8 product was limitedly employed for either scientific or practical implementations, despite its high temporal resolution. Based on a rare reference data set, this research, for the first time, verified the reliability of JMA-Himawari-8 product, and quantitatively proved that JMA-Himawari-8 product presented a large uncertainty across China and not suitable for real-time fire monitoring. In this case, NSMC-Himawari-8

515 fire products, with an hourly temporal resolution and an overall accuracy around 80 %, can be an ideal source for monitoring real-time wild fires in China. Furthermore, in recent years, with the increasing strict regulation on crop residue burning, many farmers choose to secretly burn crop residues in the nighttime, which causes a major challenge for timely monitoring and management. With the NSMC-Himawari fire products, which provides reliable 24h-hourly data sources, automatic monitoring, especially nighttime monitoring, of crop residue burning in China can be effectively implemented.

520 In previous implementations, scholars are more likely to employ official fire products released by those institutions that are operating corresponding satellites and rarely consider to originally propose a fire product based on the raw satellite data. This research is a rare attempt to produce an improved fire product based on existing raw satellite source by additionally considering localized complementary sources. The result suggested our NSMC-Himawari-8 fire product achieved a much higher accuracy than the official JMA-Himawari-8 fire product, which is not suitable for practical or research use in China.

525 By analogy, the use of complementary sources (e.g. the location of thermal sources) could further improve the local suitability of other global fire products (e.g. MODIS fire product).

Further improvement of real-time fire detection in China can be explored in the following perspectives. As introduced above, one major disadvantage of Himawari-8-based fire products is the relative coarse spatial resolution provided by Himawari-8 satellite. As an important part of Fengyun series Meteorological satellites, China plans to launch the new generation of FY-
530 4C stationary satellite with a temporal resolution of 5 minutes and an improved spatial resolution of 1km in 2024, which presents a good potential for largely enhancing the sensitivity of fire identification in China. Meanwhile, time series analysis, instead of the analysis on individual image, should be additionally considered in the algorithm of fire detection, leading to more effective removal of false fire information. With enhanced resolution and reduced uncertainty, real-time fire can be better monitored in China.

535 **6 Conclusions**

Given the uncertainty of JMA-Himawari-8 fire product in China, we proposed an adaptive hourly NSMC-Himawari-8 fire product based on the original Himawari-8 source by employing a dynamical threshold for fire-extraction and a data base of ground thermal sources. Based on the visually-extracted references and consistence check, we found NSMC-Himawari-8 fire product effectively removed a majority of false fire alarms included in the JMA-Himawari-8 fire product. Based on a rare
540 field-collected ground reference dataset, we evaluated the reliability of JMA-Himawari-8 and NSMC-Himawari-8 fire product across China. The overall accuracy of JMA-Himawari fire product was 54 % and 59 % (not considering the omission error) respectively. As a comparison, by identifying more real fire pixels and avoiding a majority of false fire alarms, the overall accuracy of NSMC-Himawari-8 fire product was 80 % and 84 % (not considering the omission errors) respectively. NSMC-Himawari-8 fire product can be a promising source for improved real-time fire monitoring across China.
545 This research also provides useful reference for employing local dataset of underlying surfaces and thermal sources to enhance the accuracy of global fire products in specific regions.

Data availability

NSMC-Himawari-8 fire product for China are available at http://figshare.com with the identifier doi: https://doi.org/10.6084/m9.figshare.21550248(Chen et al., 2022).

550 **Author Contribution**

JC, WZ, SW and CL produced NSMC-Himawari-8 fire product. JC, QL and ZC conceived the manuscript. JC, QL, ZC, WZ, YZ, CL and EZ conducted data analysis. JC, QL, XC, JY and QY produced figures. QL and ZC wrote the draft. BG produced the official website. ML, ZC and BG reviewed and revised the manuscript.

Competing interests

555 The authors have no competing interests.

Financial support

This research is supported by the National Key Research and Development Program of China (2021YFC3000300) and National Natural Science Foundation of China (Grant No.42171399).

References

560 Abram, N.J., Henley, B.J., Sen Gupta, A., Lippmann, T.J., Clarke, H., Dowdy, A.J., Sharples, J.J., Nolan, R.H., Zhang, T., and Wooster, M.J.: Connections of climate change and variability to large and extreme forest fires in southeast Australia, Communications Earth & Environment. 2, 1-17, https://doi.org/10.1038/s43247-020-00065-8, 2021.

Andela, N., Morton, D.C., Giglio, L., Chen, Y., van der Werf, G.R., Kasibhatla, P.S., DeFries, R.S., Collatz, G.J., Hantson, S., Kloster, S., Bachelet, D., Forrest, M., Lasslop, G., Li, F., Mangeon, S., Melton, J.R., Yue, C., and Randerson, J.T.: A
565 human-driven decline in global burned area, Science, 356, 1356–1362, https://doi.org/10.1126/science.aal4108, 2017.

Andersen, A.N., Cook, G.D., Corbett, L.K., Douglas, M.M., Eager, R.W., Russell-Smith, J., Setterfield, S.A., Williams, R.J., Woinarski, J.C.: Fire frequency and biodiversity conservation in Australian tropical savannas: implications from the Kapalga fire experiment, Austral ecol., 30, 155-167, https://doi.org/10.1111/j.1442-9993.2005.01441.x, 2005.

Angassa, A., and Oba, G.: Herder perceptions on impacts of range enclosures, crop farming, fire ban and bush encroachment
570 on the rangelands of Borana, Southern Ethiopia, Human ecology, 36(2), 201-215. https://doi.org/10.1007/s10745-007-9156-z, 2008.

Arino, O., Casadio, S., and Serpe, D.: Global night-time fire season timing and fire count trends using the ATSR instrument series, Remote Sens., 116, 226-238. https://doi.org/10.1016/j.rse.2011.05.025, 2012.

Balch, J.K., Bradley, B.A., D'Antonio, C.M., and Gómez-Dans, J.: Introduced annual grass increases regional fire activity across the arid western USA (1980–2009), Glob. Chang. Biol., 19, 173-183. https://doi.org/10.1111/gcb.12046, 2013.

Bessho, K., Date, K., Hayashi, M., Ikeda, A., Imai, T., Inoue, H., Kumagai, Y., Miyakawa, T., Murata, H., and Ohno, T.: An introduction to Himawari-8/9—Japan's new-generation geostationary meteorological satellites, J. Meteorol. Soc. Japan, Ser. II, 94, 151-183, https://doi.org/10.2151/jmsj.2016-009, 2016.

Chen, J., Lv, Q., Wu, S., Zeng, Y., Li, M., Chen, Z., Zhou, E., Zheng, W., Chen, X., Yang, J., and Gao, B.: NSMC-Himawari fire product for China, figshare [data set], https://doi.org/10.6084/m9.figshare.21550248, 2022.

Cascio, W. E.: Wildland fire smoke and human health, Sci. Total Environ., 624, 586-595, https://doi.org/10.1016/j.scitotenv.2017.12.086, 2018.

Chen, J., Yao, Q., Chen, Z., Li, M., Hao, Z., Liu, C., Zheng, W., Xu, M., Chen, X., Yang, J., and Lv, Q.: The Fengyun-3D (FY-3D) global active fire product: principle, methodology and validation, Earth Syst. Sci. Data, 14, 3489-3508, https://doi.org/10.5194/essd-14-3489-2022, 2022.

Chen, J., Zheng, W., Wu, S., Liu, C., and Yan, H.: Fire Monitoring Algorithm and Its Application on the Geo-Kompsat-2A Geostationary Meteorological Satellite, Remote Sens., 14(11), 2655, https://doi.org/10.3390/rs14112655, 2022.

Csiszar, I.A., Morisette, J.T., and Giglio, L.: Validation of active fire detection from moderate-resolution satellite sensors: the MODIS example in northern Eurasia, IEEE Trans. Geosci. Remote Sens., 44, 1757–1764, https://doi.org/10.1109/TGRS.2006.875941, 2006.

Cui, X., Alam, M. A., Perry, G. L., Paterson, A. M., Wyse, S. V., and Curran, T. J.: Green firebreaks as a management tool for wildfires: Lessons from China, J. Environ. Manage., 233, 329-336. https://doi.org/10.1016/j.jenvman.2018.12.043, 2019.

Driscoll, D.A., Lindenmayer, D.B., Bennett, A.F., Bode, M., Bradstock, R.A., Cary, G.J., Clarke, M.F., Dexter, N., Fensham, R., and Friend, G.: Fire management for biodiversity conservation: key research questions and our capacity to answer them, Biol. Conserv., 143, 1928-1939, https://doi.org/10.1016/j.biocon.2010.05.026, 2010.

Earl, N., and Simmonds, I.: Spatial and temporal variability and trends in 2001–2016 global fire activity, J. Geophys. Res. Atmos., 123, 2524–2536, https://doi.org/10.1002/2017JD027749, 2018.

Freeborn, P.H., Wooster, M.J., and Roberts, G.: Addressing the spatiotemporal sampling design of MODIS to provide estimates of the fire radiative energy emitted from Africa, Remote Sens. Environ., 115, 475–489, https://doi.org/10.1016/j.rse.2010.09.017, 2011.

Fuller, D. O., and Fulk, M.: Comparison of noaa-avhrr and DMSP-OLS for operational fire monitoring in kalimantan, Indonesia. Int. J. Remote Sens., 21(1), 181-187, https://doi.org/10.1080/014311600211073, 2000.

Giglio, L., Boschetti, L., Roy, D. P., Humber, M. L., and Justice, C. O.: The Collection 6 MODIS burned area mapping algorithm and product, Remote Sens. Environ., 217, 72-85, https://doi.org/10.1016/j.rse.2018.08.005, 2018.

605   Giglio, L., Csiszar, I., Justice, C.O.: Global distribution and seasonality of active fires as observed with the Terra and Aqua Moderate Resolution Imaging Spectroradiometer (MODIS) sensors, J. Geophys. Res. Biogeosci., 111, G02016, https://doi.org/10.1029/2005JG000142, 2006.

   Hall, J. V., Zhang, R., Schroeder, W., Huang, C., and Giglio, L.: Validation of GOES-16 ABI and MSG SEVIRI active fire products. Int. J. Appl. Earth. Obs. Geoinf., 83, 101928, https://doi.org/10.1016/j.jag.2019.101928, 2019.

610   Herold, M., Roberts, D.: Spectral characteristics of asphalt road aging and deterioration: implications for remote-sensing applications, Applied optics., 44(20), 4327-4334, https://doi.org/10.1364/AO.44.004327, 2005.

   Huang, X., Li, M., Li, J., and Song, Y.: A high-resolution emission inventory of crop burning in fields in China based on MODIS Thermal Anomalies/Fire products, Atmospheric Environ., 50, 9-15, https://doi.org/10.1016/j.atmosenv.2012.01.017, 2012.

615   Huff, A.K., Kondragunta, S., Zhang, H., and Hoff, R.M.: Monitoring the impacts of wildfires on forest ecosystems and public health in the exo-urban environment using high-resolution satellite aerosol products from the visible infrared imaging radiometer suite (VIIRS), Environ. Health Insights., 9s2, EHI.S19590, https://doi.org/10.4137/ehi.s19590, 2015.

   Ichoku, C., Kahn, R., and Chin, M.: Satellite contributions to the quantitative characterization of biomass burning for climate modeling. Atmos. Res., 111, 1–28, https://doi.org/10.1016/j.atmosres.2012.03.007, 2012.

620   Jacobson, M.Z.: Effects of biomass burning on climate, accounting for heat and moisture fluxes, black and brown carbon, and cloud absorption effects, J. Geophys. Res. Atmos., 119, 8980-9002, https://doi.org/10.1002/2014JD021861, 2014.

   Jang, E., Kang, Y., Im, J., Lee, D. W., Yoon, J., and Kim, S. K.: Detection and monitoring of forest fires using Himawari-8 geostationary satellite data in South Korea, Remote Sens., 11(3), 271, https://doi.org/10.3390/rs11030271, 2019.

   Johnston, F.H., Henderson, S.B., Chen, Y., Randerson, J.T., Marlier, M., DeFries, R.S., Kinney, P., Bowman, D.M., and

625   Brauer, M.: Estimated global mortality attributable to smoke from landscape fires. Environ. Health Perspect., 120, 695-701, https://doi.org/10.1289/ehp.1104422, 2012.

   Justice, C., Giglio, L., Korontzi, S., Owens, J., Morisette, J., Roy, D., Descloitres, J., Alleaume, S., Petitcolin, F., and Kaufman, Y.: The MODIS fire products. Remote Sens. Environ., 83, 244-262, https://doi.org/10.1016/S0034-4257(02)00076-7, 2002.

630   Kuenzer, C., and Dech, S.: Theoretical background of thermal infrared remote sensing, In Thermal infrared remote sensing. Springer, Dordrecht. pp. 1-26. https://doi.org/10.1007/978-94-007-6639-6_1, 2013.

   Li, F., Zhang, X., Roy, D.P., and Kondragunta, S.: Estimation of biomass-burning emissions by fusing the fire radiative power retrievals from polar-orbiting and geostationary satellites across the conterminous United States, Atmos. Environ., 211, 274–287, https://doi.org/10.1016/j.atmosenv.2019.05.017, 2019.

635   Li, J., Bo, Y., and Xie, S.: Estimating emissions from crop residue open burning in China based on statistics and MODIS fire products. J. Environ. Sci (China), 44, 158-170, https://doi.org/10.1016/j.jes.2015.08.024, 2016.

Liu, J. C., Pereira, G., Uhl, S. A., Bravo, M. A., and Bell, M. L.: A systematic review of the physical health impacts from non-occupational exposure to wildfire smoke. Environ. Res., 136, 120-132, https://doi.org/10.1016/j.envres.2014.10.015, 2015.

640 Liu, T., Marlier, M.E., DeFries, R.S., Westervelt, D.M., Xia, K.R., Fiore, A.M., Mickley, L.J., Cusworth, D.H., and Milly, G.: Seasonal impact of regional outdoor biomass burning on air pollution in three Indian cities: Delhi, Bengaluru, and Pune, Atmospheric Environ., 172, 83-92, https://doi.org/10.1016/j.atmosenv.2017.10.024, 2018.

Liu, X., He, B., Quan, X., Yebra, M., Qiu, S., Yin, C., Liao, Z., and Zhang, H.: Near real-time extracting wildfire spread rate from Himawari-8 satellite data, Remote Sens., 10(10), 1654, https://doi.org/10.3390/rs10101654, 2018.

645 Liu, Z., Yang, J., Chang, Y., Weisberg, P. J., and He, H. S.: Spatial patterns and drivers of fire occurrence and its future trend under climate change in a boreal forest of Northeast China. Glob. Chang. Biol., 18(6), 2041-2056, https://doi.org/10.1111/j.1365-2486.2012.02649.x, 2012.

Lü, A., Tian, H., and Liu, Y.: State-of-the-art in quantifying fire disturbance and ecosystem carbon cycle, Acta Ecol. Sinica., 25, 2734-2743, 2005.

650 Marlier, M.E., DeFries, R.S., Kim, P.S., Koplitz, S.N., Jacob, D.J., Mickley, L.J., and Myers, S.S.: Fire emissions and regional air quality impacts from fires in oil palm, timber, and logging concessions in Indonesia, Environ. Res. Lett., 10, 085005, https://doi.org/10.1088/1748-9326/10/8/085005, 2015.

Na, L., Zhang, J., Bao, Y., Bao, Y., Na, R., Tong, S., and Si, A.: Himawari-8 satellite based dynamic monitoring of grassland fire in China-Mongolia border regions, Sensors, 18(1), 276, https://doi.org/10.3390/s18010276, 2018.

655 Niu, R., Zhai, P.: Study on forest fire danger over Northern China during the recent 50 years. Clim. Change, 111, 723-736, https://doi.org/10.1007/s10584-011-0198-2, 2012.

Panjaitan, R. B., Sumartono, S., Sarwono, S., and Saleh, C.: The role of central government and local government and the moderating effect of good governance on forest fire policy in Indonesia, Benchmarking: An International Journal, pp. 147-159, https://doi.org/10.1108/BIJ-12-2017-0336, 2019.

660 Quinn, T. J., and Martin, J. E.: A radiometric determination of the Stefan-Boltzmann constant and thermodynamic temperatures between-40 C and+ 100 C. Philosophical Transactions of the Royal Society of London. Series A, Mathematical and Physical Sciences. 316(1536), 85-189, https://doi.org/10.1098/rsta.1985.0058, 1985.

Reid, C. E., Brauer, M., Johnston, F. H., Jerrett, M., Balmes, J. R., and Elliott, C. T.: Critical review of health impacts of wildfire smoke exposure, Environ. Health Perspect., 124(9), 1334-1343, https://doi.org/10.1289/ehp.1409277, 2016.

665 Röder, A., Hill, J., Duguy, B., Alloza, J. A., and Vallejo, R.: Using long time series of Landsat data to monitor fire events and post-fire dynamics and identify driving factors. A case study in the Ayora region (eastern Spain). Remote Sens. Environ., 112(1), 259-273, https://doi.org/10.1016/j.rse.2007.05.001, 2008.

Schmit, T.J., Griffith, P., Gunshor, M.M., Daniels, J.M., Goodman, S.J., and Lebair, W.J.: A closer look at the ABI on the GOES-R series, Bull. Am. Meteorol. Soc., 98, 681–698. https://doi.org/10.1175/bams-d-15-00230.1, 2017.

670 Schroeder, W., Csiszar, I., and Morisette, J.: Quantifying the impact of cloud obscuration on remote sensing of active fires in the Brazilian Amazon. Remote Sens. Environ., 112(2), 456-470, https://doi.org/10.1016/j.rse.2007.05.004, 2008.

Schroeder, W., Oliva, P., Giglio, L., and Csiszar, I. A.: The New VIIRS 375 m active fire detection data product: Algorithm description and initial assessment. Remote Remote Sens. Environ., 143, 85-96, https://doi.org/10.1016/j.rse.2013.12.008, 2014.

675 Sharma, A., Wang, J., Lennartson, E. M.: Intercomparison of MODIS and VIIRS fire products in Khanty-Mansiysk Russia: Implications for characterizing gas flaring from space, Atmosphere, 8(6), 95, https://doi.org/10.3390/atmos8060095.

Song, R., Wang, T., Han, J., Xu, B., Ma, D., Zhang, M., Li, S., Zhuang, B., Li, M., and Xie, M.: Spatial and temporal variation of air pollutant emissions from forest fires in China, Atmospheric Environ., 281, 119156, https://doi.org/10.1016/j.atmosenv.2022.119156, 2022.

680 Tiedemann, A.R., Klemmedson, J.O., and Bull, E.L.: Solution of forest health problems with prescribed fire: are forest productivity and wildlife at risk, For. Ecol. Manag., 127, 1-18, https://doi.org/10.1016/S0378-1127(99)00114-0, 2000.

Wang, J., Bhattacharjee, P.S., Tallapragada, V., Lu, C.H., Kondragunta, S., da Silva, A., Zhang, X., Chen, S.P., Wei, S.W., Darmenov, A.S., McQueen, J., Lee, P., Koner, P., and Harris, A.: The implementation of NEMS GFS aerosol component (NGAC) version 2.0 for global multispecies forecasting at NOAA/NCEP – part 1: model descriptions, Geosci. Model Dev., 685 11, 2315–2332. https://doi.org/10.5194/gmd-11-2315-2018, 2018.

Wang, X., Min, M., Wang, F., Guo, J., Li, B., and Tang, S.: Intercomparisons of cloud mask products among Fengyun-4A, Himawari-8, and MODIS, IEEE Transactions on Geoscience and Remote Sensing, 57(11), 8827-8839, https://doi.org/10.1109/TGRS.2019.2923247, 2019.

Wickramasinghe, C. H., Jones, S., Reinke, K., and Wallace, L.: Development of a multi-spatial resolution approach to the 690 surveillance of active fire lines using Himawari-8, Remote Sens., 8(11), 932, https://doi.org/10.3390/rs8110932, 2016.

Wu, Z., He, H. S., Yang, J., Liu, Z., and Liang, Y.: Relative effects of climatic and local factors on fire occurrence in boreal forest landscapes of northeastern China, Sci. Total Environ., 493, 472-480, https://doi.org/10.1016/j.scitotenv.2014.06.011, 2014.

Xu, G., and Zhong, X.: Real-time wildfire detection and tracking in Australia using geostationary satellite: Himawari-8. 695 Remote Sens. Lett., 8(11), 1052-1061, https://doi.org/10.1080/2150704X.2017.1350303, 2017.

Xu, W., Wooster, M.J., Kaneko, T., He, J., Zhang, T., and Fisher, D.: Major advances in geostationary fire radiative power (FRP) retrieval over Asia and Australia stemming from use of Himarawi-8 AHI. Remote Sens. Environ., 193, 138–149, https://doi.org/10.1016/j.rse.2017.02.024, 2017.

Yang, Z., Zhang, P., Gu, S., Hu, X., Tang, S., Yang, L., Xu, N., Zhen, Z., Wang, L., and Wu, Q.: Capability of Fengyun-3D 700 satellite in earth system observation, J. Meteorol. Res., 33, 1113-1130, https://doi.org/10.1007/s13351-019-9063-4, 2019.

Yang, Z.-Y., Ishii, S., Yokoyama, T., Dao, T.D., Sun, M.-G., Pankin, P.S., Timofeev, I.V., Nagao, T., and Chen, K.-P.: Narrowband wavelength selective thermal emitters by confined tamm plasmon polaritons, Acs Photonics., 4, 2212-2219, https://doi.org/10.1021/acsphotonics.7b00408, 2017.

Ying, L., Han, J., Du, Y., and Shen, Z.: Forest fire characteristics in China: Spatial patterns and determinants with thresholds, For. Ecol. Manag., 424, 345-354, https://doi.org/10.1016/j.foreco.2018.05.020, 2018.

Yuan, J., Wang, D., and Li, R.: Remote sensing image segmentation by combining spectral and texture features, IEEE Trans. Geosci. Remote Sens., 52(1), 16-24, https://doi.org/10.1109/TGRS.2012.2234755, 2014.

Zackrisson, O.: Influence of forest fires on the North Swedish boreal forest. Oikos, 22-32, https://doi.org/10.2307/3543289, 2013, 1977.

Zhang, X., and Kondragunta, S.: Temporal and spatial variability in biomass burned areas across the USA derived from the GOES fire product. Remote Sens. Environ., 112(6), 2886-2897, https://doi.org/10.1016/j.rse.2008.02.006, 2008.